PROCEEDINGS OF SPIE

LV systolic point-cloud model to quantify accuracy of CT derived regional strain

Ashish Manohar, Gabrielle Colvert, Andrew Schluchter, Francisco Contijoch, Elliot R. McVeigh

SPIE.

LV Systolic Point-Cloud Model to Quantify Accuracy of CT Derived Regional Strain

Ashish Manohar[1], Gabrielle Colvert[2], Andrew Schluchter[2], Francisco Contijoch[2,3], Elliot R. McVeigh[2,3,4]

[1] *Department of Mechanical and Aerospace Engineering, University of California San Diego, La Jolla, California, United States*

[2] *Department of Bioengineering, University of California San Diego, La Jolla, California, United States*

[3] *Department of Radiology, University of California San Diego, La Jolla, California, United States*

[4] *Department of Medicine, Cardiology Division, University of California San Diego, La Jolla, California, United States*

ABSTRACT

We present an analytical LV systolic model derived from human CT data to serve as the ground truth for optimization and validation of a previously published CT-derived regional strain metric called SQUEEZ.

Physiologically-accurate strains were applied to each vertex of a clinically derived end-diastolic LV mesh to create analytical end-systolic poses exhibiting normal function as well as regional hypokinesia of four sizes (17.5mm, 14mm, 10.5mm, and 7mm in diameter), each with a programmed severe, medium, and subtle dysfunction. Regional strain estimates were obtained by registering the end-diastolic mesh to each end-systolic mesh condition using a non-rigid registration algorithm. Ground-truth models of normal function and of severe hypokinesia were used to identify the optimal parameters in the registration algorithm, and to measure the accuracy of detecting regional dysfunction of varying sizes and severities.

We found that for normal LV systolic contraction, SQUEEZ values in all 16 AHA segments of the LV were accurately measured (within ±0.05). For cases with regional dysfunction, the errors in SQUEEZ in the region around the dysfunction increased with decreasing size of regional dysfunction. The mean SQUEEZ values of the 17.5mm and 14mm diameter dysfunctional regions, which we hypothesize are the most clinically relevant, were accurate to within ±0.05.

Keywords:
X-ray computed tomography; Cardiac imaging; Regional cardiac function; Ischemic heart disease; Cardiac modeling; Cardiac registration.

1. INTRODUCTION

The assessment of regional cardiac function has implications in the diagnosis, treatment, and follow up of patients with cardiac diseases such as myocardial ischemia[1,2], heart failure[3], cardiotoxicity[4], and dyssynchrony[5,6]. Left-ventricular (LV) ejection fraction, global longitudinal strain, and other global metrics have been useful in the assessment of overall LV function, but fail to provide information on the regional health of the myocardium. Additionally, significant reduction in global function metrics appear only in advanced disease stages whereas regional dysfunction often precedes global dysfunction.

The current gold-standard for the non-invasive assessment of regional LV function is cardiovascular magnetic resonance (CMR) tagging[7–10]. However, CMR requires long breath holds, acquisition over multiple heart beats, and manual contouring[7,11]. The growing number of patients with metallic medical device implants further limits the clinical use of CMR.

Recent advances in x-ray computed tomography (CT) have made possible the functional imaging of an entire cardiac cycle within a single heartbeat[12–16], while a static 3D image of the heart can be acquired in scan times of ~140ms. Additionally, the high spatial resolution of CT has made possible the detection and tracking of the fine LV endocardial texture comprising of trabeculae carneae[17].

SQUEEZ[17] is a new method introduced to measure regional endocardial function from 4D cine CT images acquired as per routine clinical protocols. SQUEEZ exploits the high fidelity of x-ray CT to track features of the endocardium, which are used by a non-rigid point set registration technique[18] to derive displacements of points on the endocardium across the cardiac cycle. This displacement estimate is used to obtain information on the regional strain of the endocardium. SQUEEZ has been shown to be capable of differentiating normal from dysfunctional myocardial regions in pigs[17], has been validated against CMR tagging in canines[19], and more recently, baseline estimates of SQUEEZ values in the normal functioning human LV were established[20].

The goal of this research was to establish an analytically derived LV systolic model which can serve as the ground-truth in validating and quantifying the accuracy of SQUEEZ for human hearts. Validating regional strain measures in humans is a difficult task as each imaging modality has inherent limitations, ranging from operator variability to through-plane motion, and hence the measurements maybe subject to modality-specific biases. Using the model described here, we aim to perform the first analytical evaluation of SQUEEZ in human hearts, as well as to fine tune the parameters of the registration algorithm to achieve optimal registration between the different poses of the LV across the cardiac cycle.

2. METHODS

2.1 Image Acquisition
The end-diastolic phase of a human cardiac CT scan was used as the baseline image for the development of the analytic phantom. The image was acquired under IRB approved protocols using a 320 detector-row (Aquilion ONE, Canon Medical Systems, Otawara, Japan) scanner at the National Institutes of Health (Bethesda, Maryland). Optimal opacification from contrast dye was achieved using real-time bolus tracking.

The signal-to-noise ratio (SNR) of the LV blood pool was estimated as the ratio of the mean of the Hounsfield units (HU) to the standard deviation, within a user defined region of interest (ROI). The HU within the ROI was 810 ± 44, giving an SNR of 18.4.

The image was reconstructed into a matrix of 512 x 512 x 320 voxels using the manufacturer's (Canon Medical Systems) standard reconstruction algorithm, as implemented by the clinic. The image had a resolution of 0.339 mm x 0.339 mm x 0.50 mm in the *x*, *y*, and *z* directions respectively.
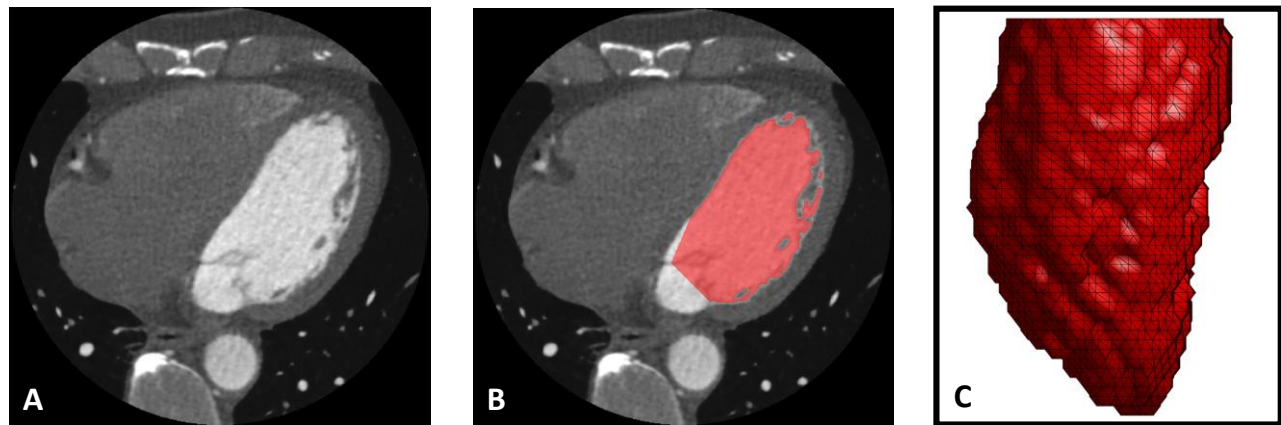
2.2 Image Processing & Mesh Extraction

The LV was segmented with ITK-SNAP[21] using the active contour region growing module (thresholding type = high pass; threshold = 450; smoothness = 10; seed radius = 5; all other parameters were set as default). All further processing steps were performed in MATLAB (MathWorks Inc.).

The binary LV segmentation was loaded into MATLAB in its native orientation and resolution. Prior to extracting the mesh, the LV binary volume was resampled to an isotropic resolution of 0.5 x 0.5 x 0.5 mm^3 through linear interpolation. The isotropic binary volume was rotated sequentially about the x and y axes, so that the LV long axis coincided with the z axis. The LV was cropped a few voxels below the mitral valve plane to obtain the mesh as an 'open' cone without a 'lid'.

The next step involved the removal of the papillary muscles. In short-axis slices, the papillary muscles appear as holes in an otherwise uniform 'circular' binary volume. In some cases, the papillary muscles form 'open holes', and filling such features is not trivial. To circumvent this problem, the binary LV blood pool was dilated using a 3x3x3 kernel. Each short-axis slice was extracted and the *imfill* in-built MATLAB routine was used to fill any holes that may be present in the slice. After filling in the papillary muscles, the binary LV was eroded back to its original state using the same 3x3x3 kernel. This process did not significantly alter the features on the mesh.

The binary LV volume was subsampled to a resolution of 2 mm x 2mm x 2mm by retaining every fourth (2mm/0.5mm) voxel in x, y, and z directions to make it consistent with previously published SQUEEZ analyses[17,19,20,22]. A mesh of the LV blood pool was extracted using the *isosurface* in-built MATLAB routine. The mesh comprised of 5257 faces and 2882 vertices. A summary of the process is shown in Fig. 1A-C.

Fig. 1. Image processing and mesh extraction. (**A**) Axial slice of the CT image. (**B**) Axial slice with the LV blood volume segmentation overlaid. (**C**) 3-D rendering of the extracted LV endocardial mesh, looking at the free wall.

2.3 Strain Model

The end-diastolic mesh, obtained from the LV segmentation as described above, was warped to an end-systolic pose by prescribing a strain model on every vertex of the point cloud. The strain model comprised of three primary components:

1. Longitudinal strain (ε_{ll})
2. Circumferential strain (ε_{cc})
3. Azimuthal rotation ($\Delta\theta$)

Azimuthal rotation is not a strain but represents the rotation of the LV endocardium during systole. For convenience, we will refer to it as the third component of the strain model. The ejection fraction of the model was 70%, which is consistent with CT based LV ejection fractions measured in normal hearts[20]. Fig. 2 shows the peak systolic values of the three components of the strain model as a function of the long axis of the LV.

2.3.1 Longitudinal strain

Longitudinal strain (ϵ_{ll}) was modeled as a constant value for every point in the LV. The value of peak end-systolic ϵ_{ll} was set to -21%[23] and prescribed to the point cloud according to the following equation

$$z_i' = z_{i-1}' + (1 + \epsilon_{ll}) * (z_i - z_{i-1}) \tag{1}$$

where z is the coordinate in the z direction, $i = 1,2,3,...,N$ is the slice number from apex to base, and z' is the new z coordinate. In this model, the terminal apical slice was fixed and all slices above compressed down towards the apex by the prescribed strain value.

2.3.2 Circumferential strain

Circumferential strain (ϵ_{cc}) was modeled as a linear reduction in strain from -44% at the apex to -34% at the base at end-systole[23]. The (x,y) coordinates were converted to polar coordinates (r,θ), with the centroid (center of LV mass) used as the center. The model was prescribed to the point cloud according to the equation

$$r_i' = r_i * (1 + \epsilon_{cc_i}) \tag{2}$$

where r is the radial coordinate, $i = 1,2,3,...,N$ is the slice number from apex to base, and r' is the new r coordinate.

2.3.3 Azimuthal rotation

Azimuthal rotation ($\Delta\theta$) was modeled as a linear decrease[24] in rotation from apex to base, with peak end-systolic rotation of 13° in the counter clockwise direction at the apex and 6.9° in the clockwise direction at the base, when viewed from apex to base[25]. As with ϵ_{cc}, the rotation model was prescribed to the point cloud in polar coordinates according to the following equation

$$\theta_i' = \theta_i + \Delta\theta_i \tag{3}$$

where θ refers to the azimuthal angle, $i = 1,2,3,...,N$ is the slice number from apex to base, and θ' is the new azimuthal angle.
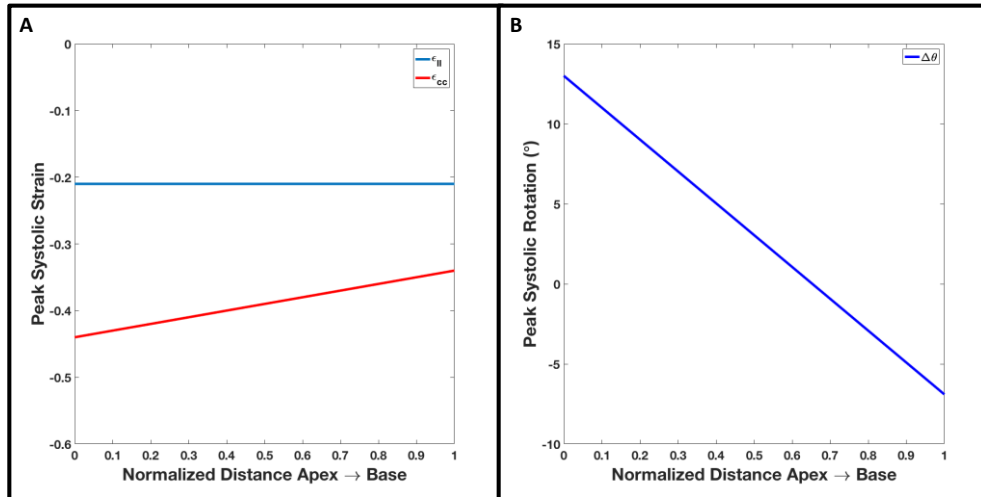
Fig 2. Components of the systolic strain model as a function of position along the LV long axis from apex (*position 0*) to base (*position 1*). (A) Peak systolic longitudinal (ϵ_{ll}, blue) and circumferential (ϵ_{cc}, red) strain functions as a function of LV long axis (B) Peak systolic LV rotation as a function of LV long axis (positive rotation is counter-clockwise when viewed from apex looking up towards the base).

2.3.4 Regional dysfunction model

Regional dysfunction was incorporated into the above strain model by prescribing a reduction factor in the ϵ_{ll} and the ϵ_{cc} components over a particular region of interest. The dysfunction model required three user input parameters:
1) Coordinates of the center of dysfunctional region
2) Diameter (size) of dysfunctional region
3) Severity of dysfunction (reduction factor in strain)

To ensure continuity of the LV tissue, a Gaussian function was imposed to ensure a smooth transition radially outward from the center (where severity is maximum) to the normal tissue. Four sizes of dysfunctional regions were simulated,

and each size was labeled as the full width at half the maximum reduction in strain of the Gaussian function. Additionally, each size was modeled with a severe, a medium, and a subtle reduction in strain. The values of strain reduction for each size was chosen through a visual inspection of meshes for physiological relevance. Table 1 summarizes the severities modeled for the different sizes.

Table 1: Severity of dysfunction for each size of dysfunction

| Diameter (mm)	Severity (% reduction in normal strain)		
	Severe	*Medium*	*Subtle*
17.5	70	50	30
14	60	45	30
10.5	50	40	30
7	40	35	30

2.3.5 Texture smoothing

To mimic the end-systolic pose of the ventricle more accurately, a low-pass filter was applied on the point cloud through the *iso2mesh*[26] MATLAB toolbox (method = 'lowpass'; iterations = 4; alpha = 0.4). This was motivated by the change in LV endocardial texture during systolic contraction[27] due to collapsing spaces between trabeculae coupled with spatial resolution limitations of the scanner. The filter is a Laplace filter applied in two steps; a forward (smoothing) step (eqn. 4) and a backward (volume conserving) step (eqn. 5) according to the following series of equations[28]

$$p' = p + \alpha \sum_{i=1}^{n} \phi(q_i - p); \qquad 0 < \alpha < 1, \phi = \frac{1}{n} \qquad (4)$$

$$p'' = p' + \mu \sum_{i=1}^{n} \phi(q_i - p); \qquad \mu = -1.02 * \alpha, \phi = \frac{1}{n} \qquad (5)$$

where p, p', and p'' are the original, intermediate, and final positions of a vertex p and $i = 1,2,3,...,n$ is the index number of the n neighboring vertices q. Fig. 3 shows the end-diastolic (Fig. 3A) and the end-systolic poses under both normal (Fig. 3B) and regional dysfunction (Fig. 3C) conditions.
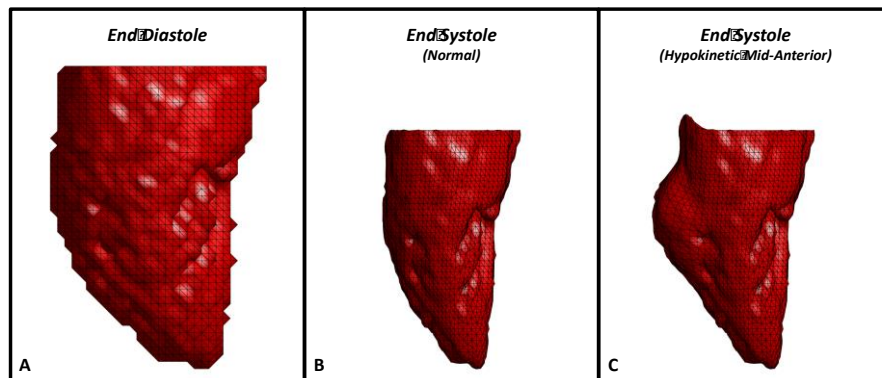
Fig. 3. End-diastolic and end-systolic poses. (**A**) End-diastolic mesh derived from human clinical CT data. (**B**) Analytically derived end-systolic pose with normal function. (**C**) Analytically derived end-systolic pose exhibiting regional hypokinesia of diameter 17.5mm at the mid-anterior segment of the LV with preserved ejection fraction in all other segments.

2.4 Non-rigid Point Set Registration

Coherent Point Drift (CPD), a probabilistic non-rigid point set registration technique[18], was used to register the end-diastolic template mesh to the end-systolic target mesh. Since our model had a perfect 1:1 correspondence, the registration accuracy can be validated with the known ground-truth. However, in the clinical scenario, a 1:1 correspondence does not exist between the end-diastolic and the end-systolic point clouds. From 10 normal human LV

scans, the ratio of the number of vertices at end-systole to end-diastole was calculated to be (mean ± SD) 46% ± 7%, and therefore, only 50% of the vertices in our analytically derived end-systolic pose were retained.

Additionally, a uniform distribution of random noise in the range of ±0.3 pixels was added to the coordinates (x, y, z) of the down-sampled end-systolic pose to decrease the overall coherence of mesh point displacement. The limits of the added noise were determined by calculating the pixel spacing (mean ± SD, 0.5 ± 0.3) between vertices in the analytically derived end-systolic mesh. This down-sampled and perturbed end-systolic pose was used as the target for the registration of the template end-diastolic mesh by CPD.

2.4.1 Identification of optimal set of CPD parameters

The registration accuracy of the CPD algorithm depends on 3 user input parameters: β, λ, and ω. β is the width of the Gaussian smoothing kernel, λ is the regularization weight, and ω parameterizes the amount of noise and expected outliers in the system[18]. Both β and λ define the coherence of motion between neighboring points; an increase in either value, forces the points to move in a more coherent manner, while lower values allow for more localized deformations.

For our application, we need the registration algorithm to balance between coherent and localized motions. The warping of the template end-diastolic mesh to the target end-systolic mesh must be performed in a physiologically accurate manner (coherent motion), while still being able to capture regional abnormalities in cardiac contraction (localized changes in the expected motions). From visual inspection trials, we identified that β values between [0.7,2] in steps of 0.1, and λ values between [1,15] in steps of 1 cover the domain of values of interest. We estimated that 1%, 5%, 10%, and 20% outliers should span the range of possible outlier fractions (ω) that occur in the clinically derived LV meshes. The above identified ranges for β, λ, and ω created 840 (14β x 15λ x 4ω) sets of possible parameters for the registration algorithm. From these 840, we sought to identify one set of parameters which yielded the *best* (defined in section 2.4.2) registration between end-diastole and end-systole under both, normal and regional dysfunction (14mm & severe; refer to Table 1.) conditions. The 14mm severe regional dysfunction model was chosen based on two factors: 1) From visual inspection of wall motion abnormalities seen on cine CT images, this seemed to be a reasonable *average* size for the optimization of the registration algorithm and 2) by optimizing for the most severe case of regional dysfunction, the registration fit would also be better capable of capturing subtle abnormalities. Furthermore, the registration algorithm may try to treat the severe dysfunction as an outlier due to the coherence seen elsewhere in the mesh.

2.4.2 Statistical evaluation

The accuracy and quality of the registration fit was assessed based on four metrics:

1) Global l^2 norm:
   The global l^2 norm was computed for all vertices of the LV according to the formula
   $$l^2_{glo} = \frac{1}{N}\sqrt{\sum_{i=1}^{N}(x_i^o - x_i)^2 + (y_i^o - y_i)^2 + (z_i^o - z_i)^2} \tag{6}$$
   where (x^o, y^o, z^o) are the coordinates of the ground-truth vertex at index i, (x, y, z) are the coordinates of the corresponding registered vertex, and $i = 1,2,3,...,2662(N)$ is the vertex index.

2) Regional l^2 norm:
   The regional l^2 norm was computed over the vertices of the dysfunctional region of the LV according to the formula
   $$l^2_{reg} = \frac{1}{n}\sqrt{\sum_{i=1}^{n}(x_i^o - x_i)^2 + (y_i^o - y_i)^2 + (z_i^o - z_i)^2} \tag{7}$$
   where (x^o, y^o, z^o) are the coordinates of the ground-truth vertex at index i, (x, y, z) are the coordinates of the corresponding registered vertex, and $i = 1,2,3,...,319(n)$ is the vertex index.

3) Euclidean distance:
   Unlike the l^2 norm which gives us an average measure of goodness of fit for all points in question, Euclidean distance was computed on a vertex by vertex basis according to the formula
   $$dist_i = \sqrt{(x_i^o - x_i)^2 + (y_i^o - y_i)^2 + (z_i^o - z_i)^2} \tag{8}$$
   where (x^o, y^o, z^o) are the coordinates of the ground-truth vertex at index i, (x, y, z) are the coordinates of the corresponding registered vertex, and $i = 1,2,3,...,2662(N)$ is the vertex index.

4) SQUEEZ:
SQUEEZ (S) is a measure of geometric strain of the endocardium at any given time t of the cardiac cycle[17], computed according to the formula

$$S = \sqrt{\frac{A(v,t)}{A(v,0)}} \qquad (9)$$

where A refers to the area of a triangular mesh element v, and t is the time frame of the cardiac cycle, $t=0$ referring to end-diastole. The area A of each triangular element v was calculated as an average area over all elements that shared one or more vertices with the element v. Additionally, from a cohort of 25 humans with normal LV function, McVeigh et al. determined the peak systolic SQUEEZ value to be 0.66 ± 0.05[20].

Among the 840 sets of parameters, only those that satisfied the following inclusion conditions were shortlisted:
1) Global l^2 norm under normal contraction ≤ 0.015 (bottom 90% of all l^2 norms; errors were consistently low)
2) Regional l^2 norm over dysfunctional vertices in the dysfunctional case ≤ 0.05 (bottom 30% of all l^2 norms)
3) 95% of SQUEEZ values under normal contraction to be within ±0.05[20] from the ground-truth
4) 90% of vertices under normal contraction to be within ± 1px. from the ground truth
5) 90% of vertices in the dysfunctional case to be within ± 1px. from the ground-truth
6) SQUEEZ value of all 16 AHA segments under normal contraction to be within ±0.05[20] from the ground-truth
7) SQUEEZ value of 15 AHA segments (excluding AHA segment 7; the mid-anterior segment containing the programed region of dysfunction) in the dysfunctional case to be within ±0.05[20] from the ground-truth
8) SQUEEZ value of AHA segment 7 in the dysfunctional case ≥ 0.75 (ground-truth value = 0.81).

2.5 Quantifying Accuracy of Detection of Regional Dysfunction
Four different sizes of dysfunctional regions, each modeled with a severe, a medium, and a subtle reduction from normal strain (see Table 1.) were used to quantify the accuracy of detection of regional dysfunction using CPD and SQUEEZ. The optimal set of CPD parameters, as determined from section 2.4.2, was used and the target end-systolic point clouds for each size and severity were prepared in the manner outlined in section 2.4 (down-sampled and perturbed).

The mean and standard deviation of the SQUEEZ values within the dysfunctional region were calculated for both the ground-truth and the registered meshes. Additionally, to understand the correlation between the ground-truth and the registered values, the mean and standard deviation of the differences in SQUEEZ were also calculated.

3. RESULTS

The results are presented under three sections: 1) Identifying the optimal set of parameters for CPD registration, 2) Quantifying accuracy of detection of various sizes and severities of regional dysfunction, and 3) Stability in measurements as a function of simulated noise.

## 3.1 Optimal Set of Parameters for CPD Registration
From the 840 sets of parameters, only 45 sets of parameters satisfied the 8 error constraints listed out in section 2.4.2. Fig. 4 shows the values of β, λ, and ω that satisfied all 8 constraints. β values between 0.9 and 1.3 satisfied the constraints; high values of β impose strong coherence of motion and hence, regional displacements (hypokinetic/infarct regions) are compromised while on the other hand, very low values of β lead to hyper-flexible meshes. The values of λ ranged from 6 to 15, the limit of our parameter search for λ. A strong inter-dependency between β and λ was also observed in Fig. 4; as the value of the width of the Gaussian smoothing kernel (β) decreased, to maintain the overall quality of the mesh (coherence of point displacements), the regularization weight (λ) had to increase. The other interesting observation was that the outlier weight ω does not alter the quality of the registration fit significantly. This made sense intuitively since our simulation was devoid of outliers.
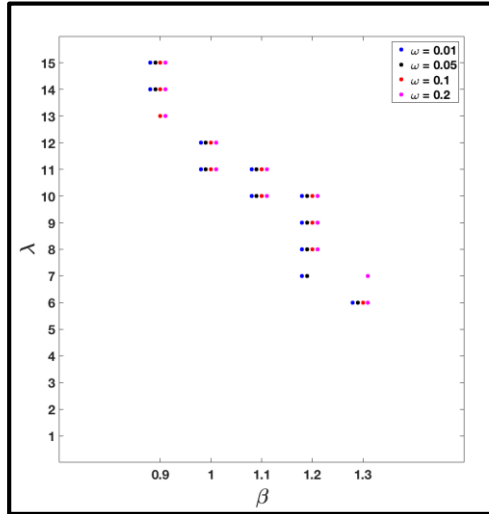
Fig. 4. β and λ values as a function of ω. Since our simulation was outlier free, the value of ω had no significant effect on the registration fit. β and λ show an inversely dependent relationship to maintain accuracy as well as coherence.

All 45 sets of parameters quantitatively performed well, satisfying the 8 established inclusion conditions. From a stability standpoint, we chose the middle set of $\beta=1.1$ and $\lambda=11$ as the operating point. Fig. 5 shows a difference map of SQUEEZ values between the theoretical and the registered meshes (theoretical – registered) under normal and regional dysfunction cases for the extreme (Fig. 5A and 5C) and the middle sets (Fig. 5B) of β and λ values as seen in Fig. 4. Neither of the meshes registered with the upper nor the lower limits of β and λ values looked significantly different from the mesh registered with the chosen middle set of β and λ values. With respect to the outlier weight, we made an educated estimate that a value of $\omega = 0.05$ is the most clinically relevant. We also hypothesize that the outlier weight will have significance in the detection of very small localized regions of dysfunction, the size of which is comparable to the outlier percentage set in the registration algorithm.
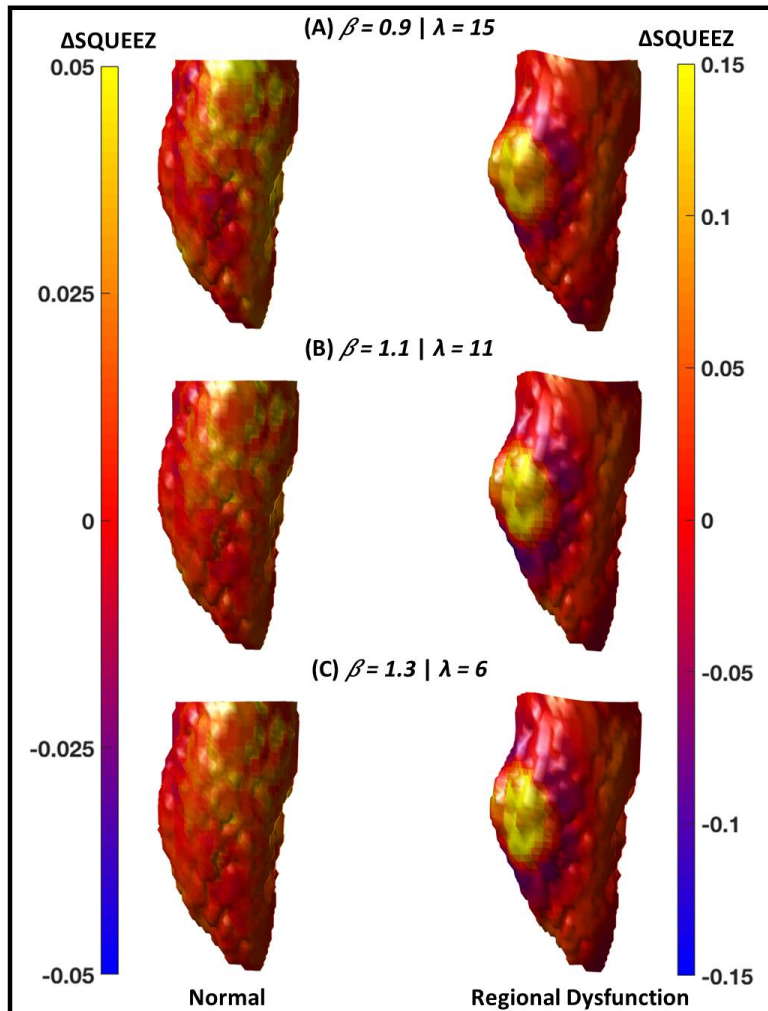
Fig. 5. Difference maps of SQUEEZ values between the theoretical and the CPD registered (theoretical – CPD) values for both normal (left column) and regional dysfunction (right column) cases (**A**) Registration performed with the upper extreme set of β and λ values as seen in Fig. 4. (**B**) Registration performed with the selected "operating point" of β and λ values as seen in Fig. 4. (**C**) Registration performed with the lower extreme set of β and λ values as seen in Fig. 4.

3.2 Accuracy of Detection of Regional Dysfunction

Four sizes of regional dysfunction were simulated with each size exhibiting a severe, a medium, and a subtle dysfunction (Table 1.). Fig. 6 shows the anterior wall of the LV for all 12 combinations (4 sizes x 3 degrees of severity) of the simulated dysfunction with the SQUEEZ values mapped onto the surface of the mesh. Panels A, B, and C show severe, medium, and subtle dysfunction respectively for the four different sizes. As a reminder, a high SQUEEZ value indicates low strain, while a low SQUEEZ value indicates good contraction. Similarly, Fig. 7 shows the CPD registered meshes with the corresponding SQUEEZ values mapped onto the surface of the mesh.
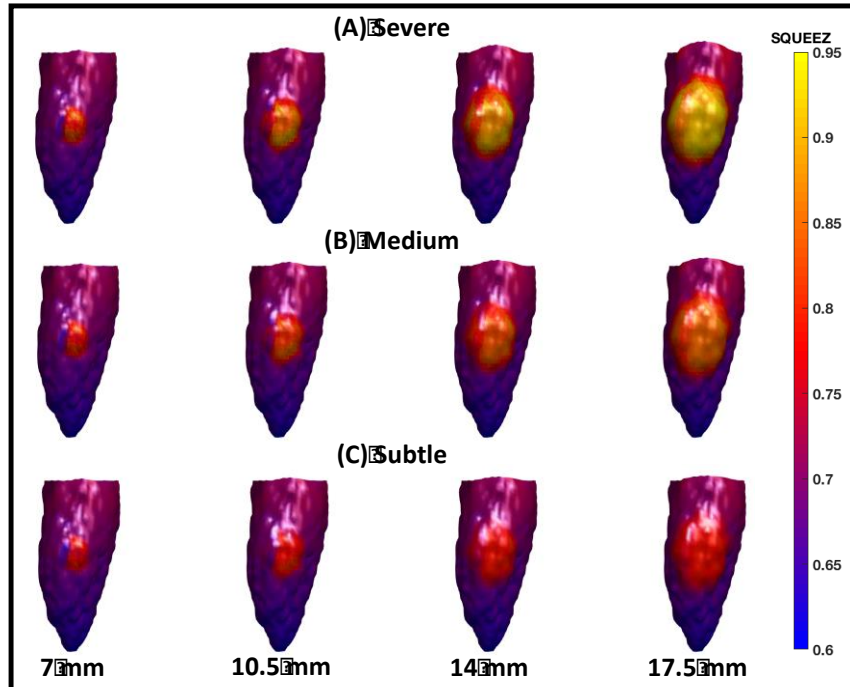
Fig. 6. Analytically derived end-systolic LV poses mapped with regional SQUEEZ values. (**A**) Severe dysfunction for each of the 4 different sizes of dysfunction. (**B**) Medium dysfunction for each of the 4 different sizes of dysfunction. (**C**) Subtle dysfunction for each of the 4 different sizes of dysfunction. Each image shows the anterior wall of the LV with the colors corresponding to the local SQUEEZ values.
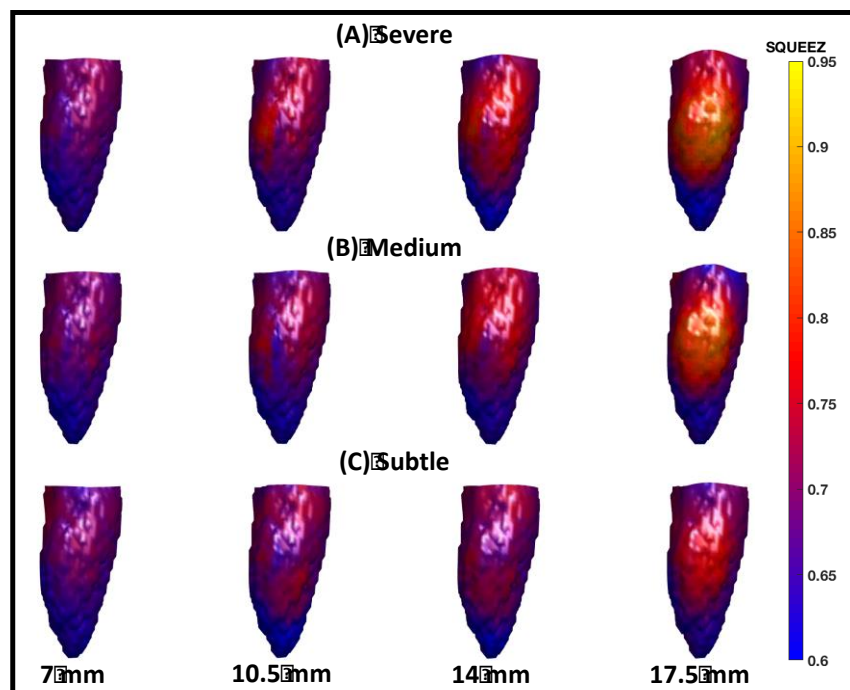
Fig. 7. CPD registered end-systolic LV poses mapped with regional SQUEEZ values. (**A**) Severe dysfunction for each of the 4 different sizes of dysfunction. (**B**) Medium dysfunction for each of the 4 different sizes of dysfunction. (**C**) Subtle dysfunction for each of the 4 different sizes of dysfunction. Each image shows the anterior wall of the LV with the colors corresponding to the local SQUEEZ values.

As seen by comparing Fig. 6 and 7, very localized and subtle abnormalities are underestimated. This was due to the emphasis on coherence of motion in the registration algorithm. A dysfunctional region of 7mm in diameter contained 25 vertices in a point cloud of 2662 vertices, which constituted for approximately 1% of the total number of vertices. This value was less than the outlier weight we used for the registration process. Acknowledging the fact that outliers will exist in the clinical cases, we need to identify a method by which we can accurately estimate the number of outliers on a case by case basis and secondly, explore the registration options further to accurately capture very small and localized regions of dysfunction like the 7mm case.

Fig. 8 quantifies the differences between the theoretical (in blue) and the CPD registered (in red) SQUEEZ values within the region of dysfunction. Fig. 8A-C show boxplots (bottom and top edges of the box correspond to the 25th and 75th percentiles and the central line indicates the median) of the distribution of SQUEEZ values within the dysfunctional region and Fig. 8D-F plot the mean difference between corresponding SQUEEZ values as a function of size with the error bars indicating to ± one standard deviation. While all three severities of dysfunction are accurately captured in the 17.5mm case, the severity of dysfunction is progressively underestimated as the size decreases. It is worth mentioning that small regions of dysfunction of size 7 and 10.5mm diameter are rarely detected by any current method in the clinical setting, however, as part of future work, we will need to further explore the registration options to accurately quantify even extremely localized and subtle wall motion abnormalities.
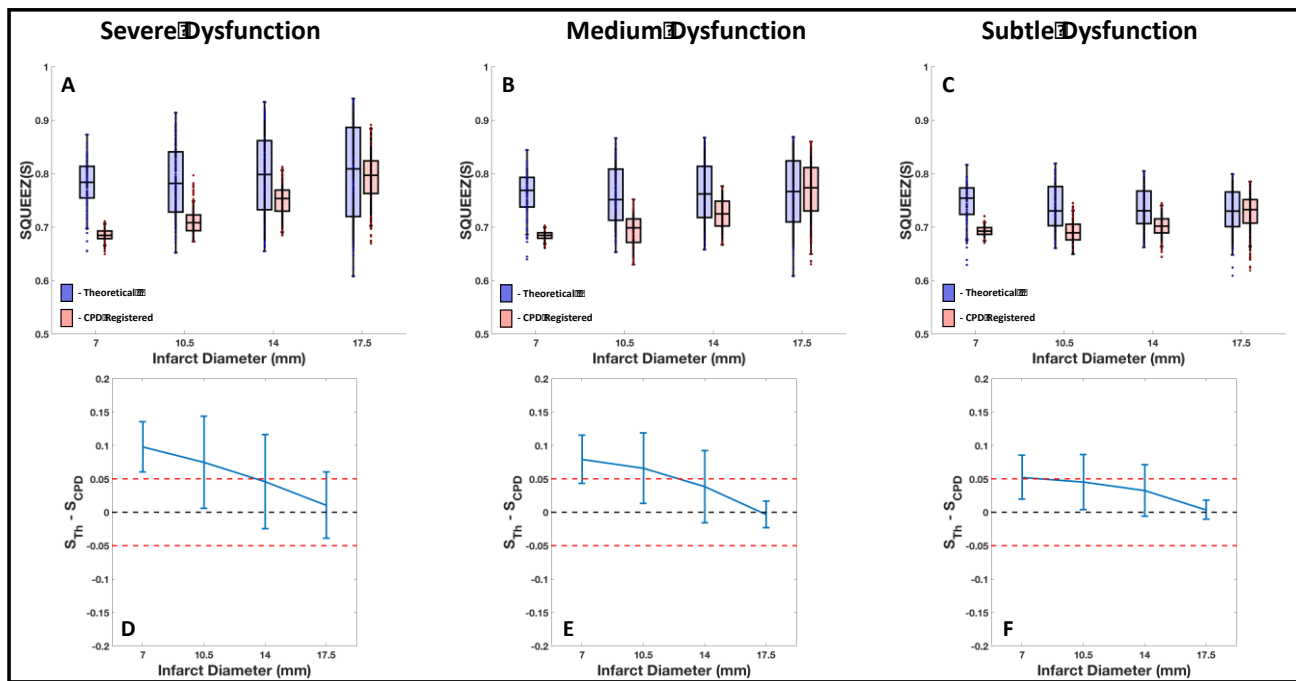
Fig. 8. Accuracy of detection of regional dysfunction through CPD and SQUEEZ. (**A-C**) Boxplots (lower and upper edge of the box correspond to the 25th and 75th percentile with the central mark indicating the median of the distribution of the theoretical (in blue) and the CPD registered (in red) SQUEEZ values within the region of dysfunction for (**A**) severe, (**B**) medium, and (**C**) subtle dysfunctions. (**D-F**) Error-bars of the mean difference (with ± one standard deviation) between the theoretical and the CPD registered SQUEEZ values within the region of dysfunction for (**D**) severe, (**E**) medium, and (**F**) subtle dysfunctions.

4. DISCUSSION

This manuscript presents a LV systolic model derived from human cardiac CT data prescribed with physiologically relevant strain functions[23–25] to create analytically known systolic poses. This is the first known LV point cloud model with programmable dysfunctional regions and the first analytical evaluation of SQUEEZ[17]. Additionally, the model makes it possible to 3D print the analytically derived systolic phases of the cardiac cycle and image them under different scanning conditions to understand the implications on LV function assessment using CT. In addition to the assessment of function, the model also provides a platform to investigate the assessment of other LV phenomena such as dyssynchrony and twist.

Using a model for normal LV function and a model for regional dysfunction of moderate size and severity, the most optimal set of parameters for the CPD[18] registration algorithm were identified. This was the first attempt at identifying the optimal set of parameters for the quantification of human regional LV function using SQUEEZ. With these parameters, the accuracy of detecting programmed dysfunctional regions using the CPD and SQUEEZ pipeline was quantified. The accuracy decreased as a function of decreasing size, with almost perfect detection for the region of diameter 17.5mm and severe underestimation of dysfunction for the very small dysfunctional region of 7mm in diameter.

While the spatial resolution of detecting regional dysfunction was established, future work is necessary to improve the accuracy to enable the detection of very small localized regions of dysfunction. Additionally, the effect of spatial resolution on the accuracy of point-cloud registration and SQUEEZ needs to be investigated.

4.1 Limitations

While the model served as a ground-truth in the validation and fine-tuning of the CPD and SQUEEZ pipeline of measuring regional LV function, it does not accurately represent the texture change of the human LV during systolic contraction. Although a low-pass filter was applied to break feature correspondence, human LV systolic contraction loses features in a non-coherent fashion.

Currently, regional dysfunction is modeled in a circular pattern, with the most severe dysfunction at the center and a gradual tapering off towards normal function radially outward. The model is limited by its symmetric shape; regional dysfunction occurs in various shapes, often in a non-isotropic manner. The accuracy of detection of regional dysfunction with non-isotropic spatial scales in *x, y,* and *z* needs to be investigated.

While the model offers a great deal of flexibility in programming regional dysfunction, it is currently limited by the fact that it does not incorporate an accurate model of CT noise in the independent phases of LV contraction. Future work should address the effects of increasing CT noise (with reduced patient dose) and outliers on the computed SQUEEZ values.

ACKNOWLEDGEMENTS

REFERENCES

[1] Amundsen, B. H., Helle-Valle, T., Edvardsen, T., Torp, H., Crosby, J., Lyseggen, E., Støylen, A., Ihlen, H., Lima, J. A. C., Smiseth, O. A. and Slørdahl, S. A., "Noninvasive myocardial strain measurement by speckle tracking echocardiography: Validation against sonomicrometry and tagged magnetic resonance imaging," J. Am. Coll. Cardiol. **47**(4), 789–793 (2006).

[2] Moore, C. C., McVeigh, E. R. and Zerhouni, E. A., "Noninvasive Measurement of Three-Dimensional Myocardial Deformation with Tagged Magnetic Resonance Imaging during Graded Local Ischemia," J. Cardiovasc. Magn. Reson. **1**(3), 207–222 (1999).

[3] Cho, G. Y., Marwick, T. H., Kim, H. S., Kim, M. K., Hong, K. S. and Oh, D. J., "Global 2-Dimensional Strain as a New Prognosticator in Patients With Heart Failure," J. Am. Coll. Cardiol. **54**(7), 618–624 (2009).

[4] Thavendiranathan, P., Poulin, F., Lim, K. D., Plana, J. C., Woo, A. and Marwick, T. H., "Use of myocardial strain imaging by echocardiography for the early detection of cardiotoxicity in patients during and after cancer chemotherapy: A systematic review," J. Am. Coll. Cardiol. **63**(25 PART A), 2751–2768 (2014).

[5] Leclercq, C., Faris, O., Tunin, R., Johnson, J., Kato, R., Evans, F., Spinelli, J., Halperin, H., McVeigh, E. and Kass, D. A., "Systolic improvement and mechanical resynchronization does not require electrical synchrony in the dilated failing heart with left bundle-branch block," Circulation **106**(14), 1760–1763 (2002).

[6] Prinzen, F. W., Hunter, W. C., Wyman, B. T. and McVeigh, E. R., "Mapping of regional myocardial strain and work during ventricular pacing: Experimental study using magnetic resonance imaging tagging," J. Am. Coll. Cardiol. **33**(6), 1735–1742 (1999).

[7] Ibrahim, E.-S. H., "Myocardial tagging by Cardiovascular Magnetic Resonance: evolution of techniques--pulse sequences, analysis algorithms, and applications," J. Cardiovasc. Magn. Reson. **13**(1), 36 (2011).

[8] Jeung, M.-Y., Germain, P., Croisille, P., ghannudi, S. El, Roy, C. and Gangi, A., "Myocardial Tagging with MR Imaging: Overview of Normal and Pathologic Findings," RadioGraphics **32**(5), 1381–1398 (2012).

[9] Ozturk, C., Derbyshire, J. A. and Mcveigh, E. R., "Estimating motion from MRI data," Proc. IEEE **91**(10), 1627–1647 (2003).

[10] Wang, H. and Amini, A. A., "Cardiac motion and deformation recovery from MRI: A review," IEEE Trans. Med. Imaging **31**(2), 487–503 (2012).

[11] McVeigh, E. R., "Regional Myocardial Functon," Cardiol. Clin. **16**(2), 189–206 (1998).

[12] Choi, S. Il, George, R. T., Schuleri, K. H., Chun, E. J., Lima, J. A. C. and Lardo, A. C., "Recent developments in wide-detector cardiac computed tomography," Int. J. Cardiovasc. Imaging **25**(SUPPL. 1), 23–29 (2009).

[13] Kitagawa, K., Lardo, A. C., Lima, J. A. C. and George, R. T., "Prospective ECG-gated 320 row detector computed tomography: Implications for CT angiography and perfusion imaging," Int. J. Cardiovasc. Imaging **25**(SUPPL. 2), 201–208 (2009).

[14] Rybicki, F. J., Otero, H. J., Steigner, M. L., Vorobiof, G., Nallamshetty, L., Mitsouras, D., Ersoy, H., Mather, R. T., Judy, P. F., Cai, T., Coyner, K., Schultz, K., Whitmore, A. G. and Di Carli, M. F., "Initial evaluation of coronary images from 320-detector row computed tomography," Int. J. Cardiovasc. Imaging **24**(5), 535–546 (2008).

[15] Schuleri, K. H., George, R. T. and Lardo, A. C., "Applications of cardiac multidetector CT beyond coronary angiography," Nat. Rev. Cardiol. **6**(11), 699–710 (2009).

[16] Steigner, M. L., Otero, H. J., Cai, T., Mitsouras, D., Nallamshetty, L., Whitmore, A. G., Ersoy, H., Levit, N. A., Di Carli, M. F. and Rybicki, F. J., "Narrowing the phase window width in prospectively ECG-gated single heart beat 320-detector row coronary CT angiography," Int. J. Cardiovasc. Imaging **25**(1), 85–90 (2009).

[17] Pourmorteza, A., Schuleri, K. H., Herzka, D. A., Lardo, A. C. and McVeigh, E. R., "A new method for cardiac computed tomography regional function assessment: Stretch quantifier for endocardial engraved zones (SQUEEZ)," Circ. Cardiovasc. Imaging **5**(2), 243–250 (2012).

[18] Myronenko, A. and Song, X., "Point set registration: coherent point drift.," IEEE Trans. Pattern Anal. Mach. Intell. **32**(12), 2262–2275 (2010).

[19] Pourmorteza, A., Chen, M. Y., Pals, J. van der, Arai, A. E. and McVeigh, E. R., "Correlation of CT-based regional cardiac function (SQUEEZ) with myocardial strain calculated from tagged MRI: an experimental study," Int. J. Cardiovasc. Imaging **32**(5), 817–823 (2016).

[20] McVeigh, E. R., Pourmorteza, A., Guttman, M., Sandfort, V., Contijoch, F., Budhiraja, S., Chen, Z., Bluemke, D. A. and Chen, M. Y., "Regional myocardial strain measurements from 4DCT in patients with normal LV function," J. Cardiovasc. Comput. Tomogr. **12**(5), 372–378 (2018).

[21]   Yushkevich, P. A., Piven, J., Hazlett, C., Smith, G., Ho, S., Gee, J. C. and Gerig, G., "User-guided 3D active contour segmentation of anatomical structures : Significantly improved efficiency and reliability," Neuroimage **31**(3), 1116–1128 (2006).

[22]   Contijoch, F. J., Groves, D. W., Chen, Z., Chen, M. Y. and McVeigh, E. R., "A novel method for evaluating regional RV function in the adult congenital heart with low-dose CT and SQUEEZ processing," Int. J. Cardiol. **249**, 461–466 (2017).

[23]   Shi, J., Pan, C., Kong, D., Cheng, L. and Shu, X., "Left Ventricular Longitudinal and Circumferential Layer-Specific Myocardial Strains and Their Determinants in Healthy Subjects," Echocardiography **33**(4), 510–518 (2016).

[24]   Moore, C. C., Lugo-Olivieri, C. H., McVeigh, E. R. and Zerhouni, E. A., "Three-dimensional Systolic Strain Patterns in the Normal Human Left Ventricle: Characterization with Tagged MR Imaging," Radiology **214**(2), 453–466 (2000).

[25]   Kocabay, G., Muraru, D., Peluso, D., Cucchini, U., Mihaila, S., Padayattil-Jose, S., Gentian, D., Iliceto, S., Vinereanu, D. and Badano, L. P., "Normal left ventricular mechanics by two-dimensional speckle-tracking echocardiography. Reference values in healthy adults.," Rev. Esp. Cardiol. (Engl. Ed). **67**(8), 651–658 (2014).

[26]   Fang, Q. and Boas, D., "Tetrahedral mesh generation from volumetric binary and gray-scale images," Proc. IEEE Int. Symp. Biomed. Imaging, 1142–1145 (2009).

[27]   Moore, B. and Prasad Dasi, L., "Quantifying left ventricular trabeculae function - application of image-based fractal analysis.," Physiol. Rep. **1**(4), e00068 (2013).

[28]   Bade, R., Haase, J. and Preim, B., "Comparison of Fundamental Mesh Smoothing Algorithms for Medical Surface Models," SimVis **6**, 289–304 (2006).